Original Paper

Efficient aerobic oxidative desulfurization via three-dimensional ordered macroporous tungsten-titanium oxides

Ming Zhang [a, *], Yu-Jie Fu [a], Chao Wang [b], Yan-Chen Wei [a], Yong-Kang Gao [a], Wen-Shu Yang [a], Lei Fan [c], Wen-Shuai Zhu [a, **], Hua-Ming Li [a, ***]

[a] Institute for Energy Research, School of Chemistry and Chemical Engineering, Jiangsu University, Zhenjiang, 212013, PR China
[b] Institute of Environmental Health and Ecological Security, School of the Environment and Safety Engineering, Jiangsu University, Zhenjiang, 212013, PR China
[c] School of Chemistry and Chemical Engineering, Yangzhou University, Yangzhou, 225002, PR China

ARTICLE INFO

ABSTRACT

A series of three-dimensional ordered macroporous (3DOM) W—TiO$_2$ catalysts have been prepared through a facile colloidal crystal template method. The prepared materials characterized in detail exhibited enhanced catalytic activity in aerobic oxidative desulfurization process. The experimental results indicated that the as-prepared materials possessed excellent 3DOM structure, which is beneficial for the catalytic activity. The sample 3DOM W—TiO$_2$-20 exhibited the highest activity in ODS process, and the sulfur removal can reach 98% in 6 h. Furthermore, the oxidative product was also analyzed in the reaction process.

1. Introduction

The reduction of SO$_x$ emission is increasingly urgent because of pollution control and human health concerns in the worldwide. Sulfur compounds existing in the petroleum are the main source of SO$_x$ discharged to the air (Chi et al., 2020; Wei et al., 2020). With the stringent regulations on the limitation of SO$_x$ emission, hydrodesulfurization (HDS) is considered as the traditional desulfurization technology in industry (Cao et al., 2020; Saleh et al., 2019; Yuan et al., 2014), which can effectively remove most of the sulfides such as mercaptans and thioethers (Hao et al., 2019; Tan et al., 2017; Xiao et al., 2014). However, the removal efficiency towards aromatic sulfides such as dibenzothiophene (DBT) and its derivatives is unsatisfied in this procedure (Jiang et al., 2016; Xun et al., 2019; Zhang et al., 2013). Therefore, non-hydrodesulfurization technologies

were also developed including oxidative desulfurization (Chen et al., 2017; Zhang et al. 2017, 2020), adsorptive desulfurization (Ahmed and Jhung, 2016; Dong et al., 2020; Xiong et al., 2016), extractive desulfurization (Li et al., 2016; Song et al., 2017; Wang J. et al., 2020), and biological desulfurization (Sousa et al., 2020). Among them, oxidative desulfurization (ODS) has attracted wide attentions due to its high desulfurization efficiency and mild operating conditions. In ODS process, various kinds of oxidants have been studied such as organic peroxyacid, H$_2$O$_2$, NaClO, and O$_2$ (Li et al., 2020; Xu et al., 2020). Notably, O$_2$ abundant in the air could be a good candidate for ODS process under atmospheric condition.

The selection of catalysts is one of the most important factors in a catalytic reaction. A suitable catalyst can shorten the reaction time and lower the reaction temperature. Transition metals with unique physicochemical properties are often used as catalysts in various kinds of oxidative reactions (Chen et al., 2017; Pei et al., 2020; Wang et al., 2021; Xie et al., 2015). Especially, W (VI) in tungsten oxide based materials can be reduced to its low valence states including W (V) or W (IV) (He et al., 2017; Sun et al., 2018). These tungsten atom at low valence can activate the oxidant to form the peroxide specie, which is a kind of strong oxidizing intermediate in the ODS process (Yang et al., 2018; Yang H. et al.,

* Corresponding author.
** Corresponding author.
*** Corresponding author.
E-mail addresses: zm@ujs.edu.cn (M. Zhang), zhuws@ujs.edu.cn (W.-S. Zhu), lhm@ujs.edu.cn (H.-M. Li).

2017). Hence, transition metals (e.g. tungsten, molybdenum and vanadium) can be employed as active centers with a suitable carrier (Xun et al., 2016). Du et al. synthesized HPW/TiO$_2$ catalysts using titanium dioxide as the carrier for activating hydrogen peroxide in the oxidative desulfurization (Du et al., 2018). In the oxidative reaction, titanium dioxide is also a kind active center. Metal doping can change the crystal structure of titanium dioxide, thereby improving the oxidative properties of materials. Especially, the atomic radius (0.61 Å) of W^{6+} is similar to that of Ti^{4+} (0.62 Å). Hence, tungsten might be an ideal dopant for titanium dioxide.

Due to the open porous, interconnected macro-porous structure and nano-sized pore walls, three-dimensional ordered macroporous (3DOM) structure in the catalyst is beneficial for the entry of reactants into pores from all directions, which can reduce the resistance during reaction, and provide a maximum flow rate and increased mass transportation efficiency (Pei et al., 2020; Wu et al., 2019; Xie et al., 2015; Zalfani et al., 2016). For solid catalysts, their specific surface area and interface can be improved via the introduction of porous structure. The increased specific surface area is beneficial for the exposure of catalytic active sites, enhancing the collision frequency between reactants and active sites. At the same time, the increased pore volume and limited curvature in the porous materials could generally improve the transfer and diffusion of the reactants. Hence, 3DOM materials are suitable for heterogeneous catalytic reactions, obtaining moderate specific surface area through large pores and complete interconnection of pores.

In this work, a series of hybrid materials 3DOM W–TiO$_2$ were successfully prepared via the colloidal crystal template method, and employed as catalysts in the aerobic oxidative desulfurization. The prepared materials would take advantage of both transition metal and 3DOM materials. The prepared samples characterized in detail exhibited efficient performance in aerobic ODS process as well as the recycling ability. Moreover, the reaction product of sulfur compounds was also studied according to GC-MS analysis. The successful construction of 3DOM W–TiO$_2$ would bring new opportunities for the rational design of 3DOM materials with enhanced catalytic oxidative performance.

2. Experimental section

2.1. Materials

Methyl methacrylate (99%), ammonium metatungstate (99.5%), hexadecane (98%) and 4,6-dimethyldibenzothiphene (4,6-DMDBT, 97%) were purchased from Aladdin Chemistry Co., Ltd. Titanium tetraisopropanolate (97%), dibenzothiophene (DBT, 98%) and 4-

$$\text{Sulfur removal } (\%) = \frac{\text{Initial sulfur content } - \text{ Residual sulfur content}}{\text{Initial sulfur content}} \times 100\%$$

methyldibenzothiophene (4-MDBT, 96%) were obtained from Sigma Aldrich Trading Co., Ltd. Dodecane was marketed by Macklin Biochemical Technology Co., Ltd. Potassium persulfate (AR grade), hydrochloric acid (HCl, AR grade) and ethanol (EtOH, AR grade) were obtained from Sinopharm Chemical Reagents Co., Ltd.

2.2. Synthesis of samples

The polymethyl methacrylate (PMMA) microspheres with a size of 250 nm were prepared according to previous study (Celestine

et al., 2014). At room temperature, a certain amount of ethanol, hydrochloric acid, titanium tetraisopropanolate and ammonium metatungstate solution with corresponding concentration were added to the beaker successively with constant stirring. Then, the template PMMA was added to the above mixture. After the removal of the excess liquid, the obtained solid was dried at room temperature for 48 h, transferred to the muffle furnace and calcinated at 300 °C for 2 h, 400 °C for 2 h and 550 °C. For comparison, a series of samples were prepared with different Ti/W molar ratios and noted as 3DOM W–TiO$_2$-X (X = 10, 20 and 30), where X represented the Ti/W molar ratio. In addition, 3DOM TiO$_2$ without tungsten source was also synthesized with the same method.

2.3. Characterization

Scanning emission microscopy (SEM) was conducted using a JSM-7800F Microscope. Transmission electron microscopy (TEM) was carried out over a JEM 2100 (HR) Microscope operating at 200 kV. High resolution transmission electron microscopy (HR-TEM) was recorded using a Tecnai G2 F30 S-TWIN Microscope. The X-ray diffraction (XRD) analysis was carried out over a D8 diffractometer using Cu-Kα radiation with a scan rate of 7°/min in the range of 10°–80°. Fourier transformed infrared (FT-IR) spectra were recorded on a Nicolet iS-50 spectrometer with the samples prepared in the form of KBr pellets. Raman spectra were conducted over a DXR Raman microscope using a 532 nm laser for excitation. Nitrogen adsorption-desorption isotherms were acquired on a Tristar II 3020 apparatus. X-ray photoelectron spectroscopy (XPS) characterization was acquired on a Thermo ESCALAB 250Xi spectrometer, equipped with a monochromatic Al Kα source.

2.4. Oxidative desulfurization process

The model oil was prepared by dissolving DBT, 4-MDBT and 4,6-DMDBT in dodecane with a corresponding S-concentration of 200 ppm respectively. In a typical reaction process, 0.01 g of the prepared samples and 20 mL of model oil was added in a three-necked flask equipped with a magnetic stirrer and a heater set at a certain temperature. Then, the air was injected to reactor at a flow rate of 100 mL/min. The residual sulfur content in the model oil was determined by gas chromatography on Shimadzu GC 2010 Plus (SH-Rtx-5, 30 m × 0.25 mm × 0.25 μm). The injector temperature was 250 °C, and the detector temperature was 300 °C. The temperature of the GC process started at 100 °C and rose to 250 °C at 25 °C/min. The sulfur removal (%) was calculated by the formula as follows:

3. Results and discussion

3.1. Characterization of samples

FT-IR spectroscopy of the prepared samples is presented in Fig. 1. The adsorption in the range of 400–800 cm^{-1} was ascribed to the vibration peak of Ti–O–Ti, indicating the formation of Ti–O band in the synthesis procedure (Ye et al., 2018). For the sample 3DOM W–TiO$_2$-10, the peak around 980 cm^{-1} could be clearly observed, which was attributed to ν$_{as}$ (W=O) (Yang P. et al., 2017). As Ti/W
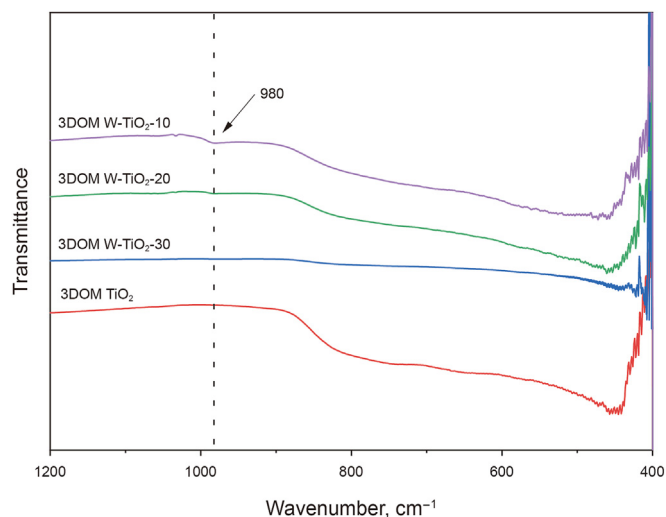
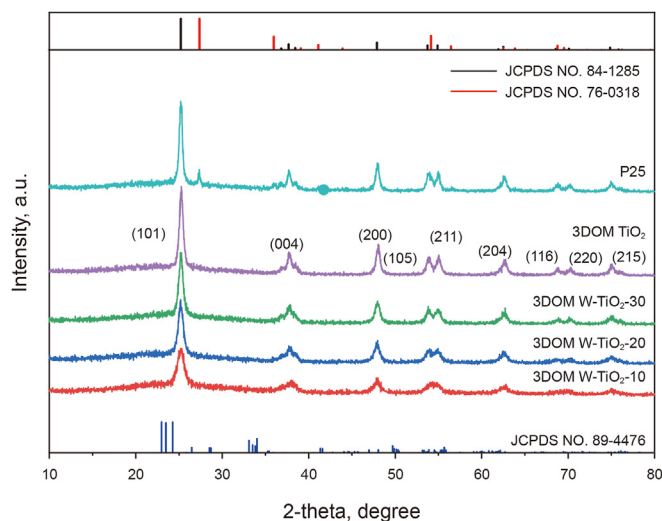**Fig. 1.** FT-IR spectra of the as-prepared materials.

Fig. 3. Wide XRD patterns of various materials.

molar ratio increased, the tungsten contents gradually decreased, resulting in the decreased intensity of the W=O peak. These results demonstrated the successful preparation of hybrid material W−TiO$_2$.

To further study the structural information, Raman scattering spectroscopy of the various samples is presented in this study (Fig. 2). As seen in Fig. 2a, the characteristic peaks of the 3DOM TiO$_2$ were well consistent with the peaks of the commercial titanium dioxide (P25). In addition, Fig. 2b was obtained by amplifying the area of 900−1100 cm^{-1} in Fig. 2a. For the samples 3DOM W−TiO$_2$-5, the characteristic peaks of can be obviously found around 982 cm^{-1}, indicating the presence of tungsten in the sample (Colusso et al., 2017). When the value of Ti/W increased, the intensity of the characteristic peak ν (W=O) gradually decreased. For the samples 3DOM W−TiO$_2$-30, the vibration peak of W=O could

be hardly observed with a low content of tungsten. These results from the Raman spectra also indicated the successful synthesis of hybrid material W−TiO$_2$.

To study the intrinsic structure of the prepared samples, wide XRD patterns are depicted in this study (Fig. 3). For the commercial P25, the characteristic peaks for the anatase TiO$_2$ (JCPDS: 84−1285) and rutile TiO$_2$ (JCPDS: 76−0318) could be found. For the sample 3DOM TiO$_2$, a series of characteristic peaks for (101), (004), (200), (105), (211), (204), (116), (220) and (215) crystal planes ascribed to anatase TiO$_2$ were observed at 25.2°, 37.7°, 48.1°, 53.9°, 68.7°, 70.3° and 5.0°, respectively. After the introduction of tungsten with different contents, anatase TiO$_2$ structure could also be found for the 3DOM TiO$_2$ samples. However, no obvious diffraction peak for tungsten was found, which was ascribed to high dispersion of tungsten in the support TiO$_2$ (Ullah et al., 2018; Wang C. et al.,
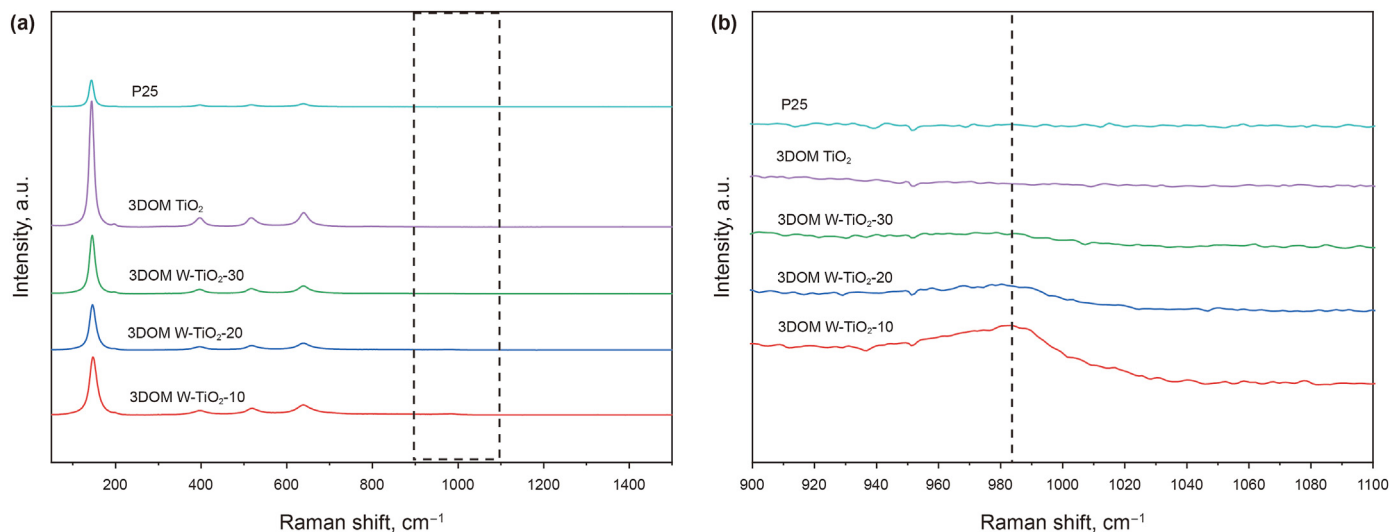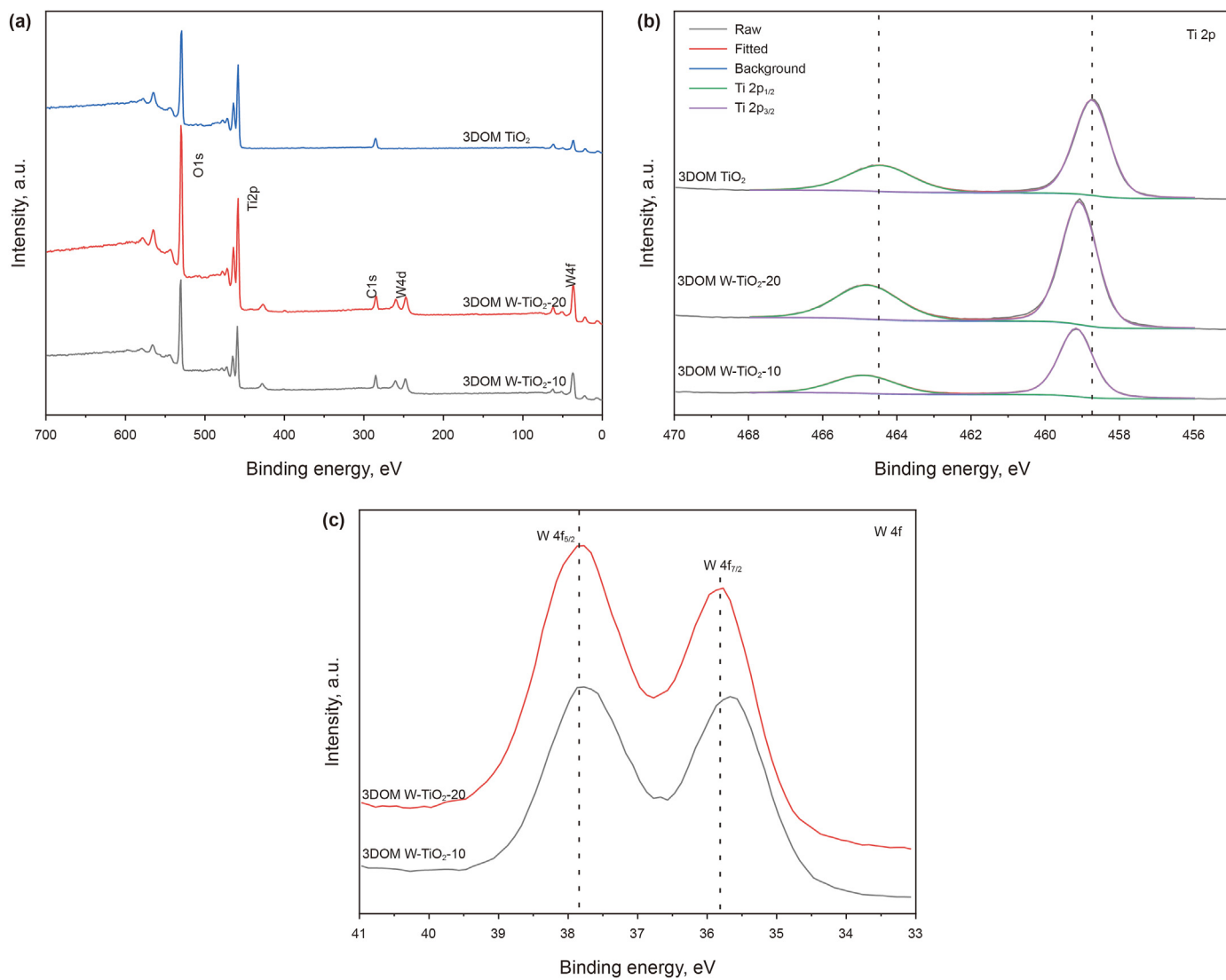

Fig. 2. Raman spectra of the as-prepared materials.

Fig. 4. The XPS spectrum of **a** survey, **b** Ti2p core-level spectra and **c** W4f core-level spectra.
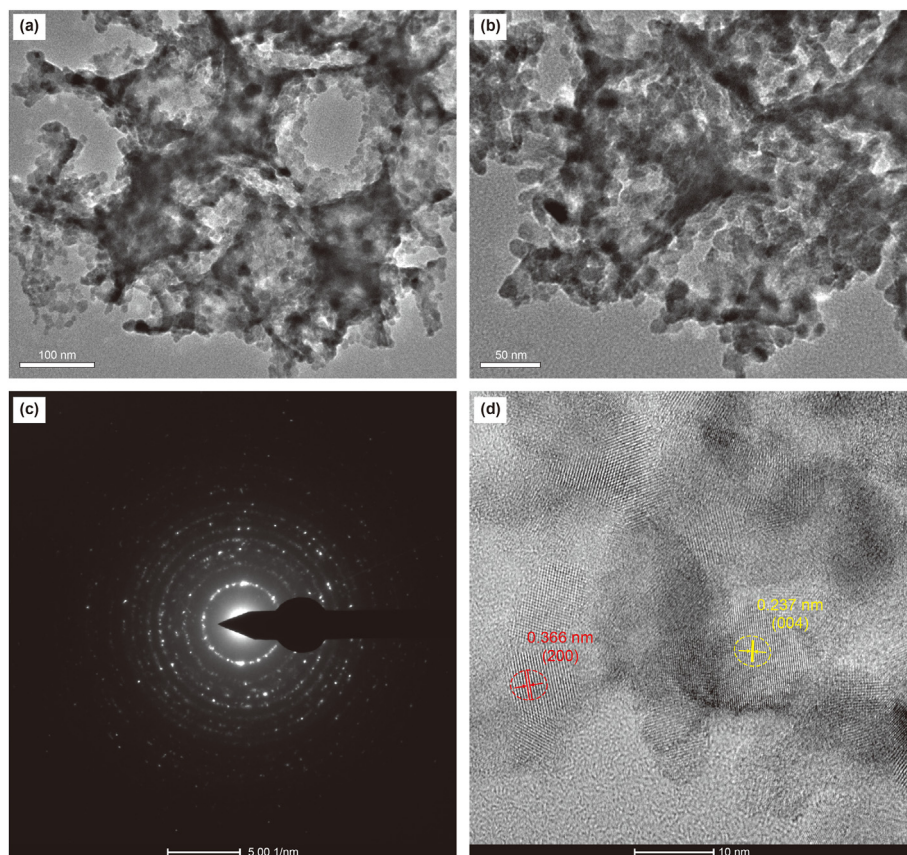
Fig. 5. a, **b** TEM images, **c** SAED image and **d** HR-TEM image of 3DOM W−TiO$_2$-20.

2020b). These results indicated that the tungsten was successfully introduced to titanium dioxide with a high dispersion.

To further explore the chemical environment and compositions in the samples, XPS spectra of 3DOM TiO$_2$, 3DOM W−TiO$_2$-20 and W-3DOM TiO$_2$-10 are conducted (Fig. 4). In Fig. 4a, the peaks around 530, 458, 285, 246 and 37 eV ascribed to the O1s, Ti2p, C1s, W4d and W4f could be observed respectively, indicating the existence of tungsten and titanium oxide in the sample. In Fig. 4b, Ti2p$_{1/2}$ and Ti2p$_{3/2}$ spectra of 3DOM TiO$_2$ could detected around 464.4 eV and 458.7 eV, indicating the existence of Ti (IV) (Ye et al., 2018). Notably, Ti2p$_{1/2}$ and Ti2p$_{3/2}$ curves of the samples 3DOM W−TiO$_2$-20 and 3DOM W−TiO$_2$-10 were detected around 464.8 eV, 459.1 eV and 464.9 eV, 459.2 eV, respectively. Compared to that of 3DOM TiO$_2$, the characteristic peaks of 3DOM W−TiO$_2$-20 and 3DOM W−TiO$_2$-10 shifted to a higher binding energy, indicating the successful doping of tungsten (Cong et al., 2011). In Fig. 4c, the W4f$_{5/2}$ and W4f$_{7/2}$ spectra of the sample 3DOM W−TiO$_2$-20 and 3DOM W−TiO$_2$-10 were detected at 37.9 eV, 35.8 eV and 37.8 eV, 35.7 eV respectively, indicating the existence of W^{6+} (Xie et al., 2018).

To further study the morphology and composition of the samples, TEM and HR-TEM images are employed for the typical sample 3DOM W−TiO$_2$-20 (Fig. 5). In Fig. 5a and b, the light gray part was ascribed to the pore as well as the black part for the pore wall, which was mostly composed of titanium oxide crystal grains. For the selected area electron diffraction pattern of the catalyst

(Fig. 5c), 3DOM W−TiO$_2$-20 exhibits a polycrystal structure, which was well consistent with the results of XRD analysis. Besides, the HR-TEM technique was applied to verify the presence of tungsten in the sample (Fig. 5d). The lattice spacing in the yellow dotted circle was 0.237 nm, which was attributed to the (004) crystal plane of anatase TiO$_2$ (Chen et al., 2014). The red dotted circle was 0.366 nm, corresponding to the (200) crystal plane of WO$_3$ (Shen et al., 2018). Subsequently, TEM-mapping analysis was carried out to probe the presence and distribution of tungsten in the sample (Fig. 6). The uniformed distribution of elements O, Ti and W were observed, further demonstrating the successful doping of tungsten with a high dispersion.

In order to investigate the pore structure properties of the samples, N$_2$ adsorption and desorption analysis is employed in this study (Fig. 7). All the samples exhibited type II isotherms with H3 hysteresis loops (Soltani et al., 2019). Besides, the adsorption curves of the samples sharply increased around P/P$_0$ = 1, while no adsorption platform was found, also indicating the existence of macro-porous structure. Moreover, the specific surface area and pore volume of the samples are provided in Table 1. It could be found that the pore volume decreased as the tungsten content increased in the samples. The specific surface area of the samples also slightly decreased, indicating that the pore structure was not obviously affected after the introduction of tungsten.
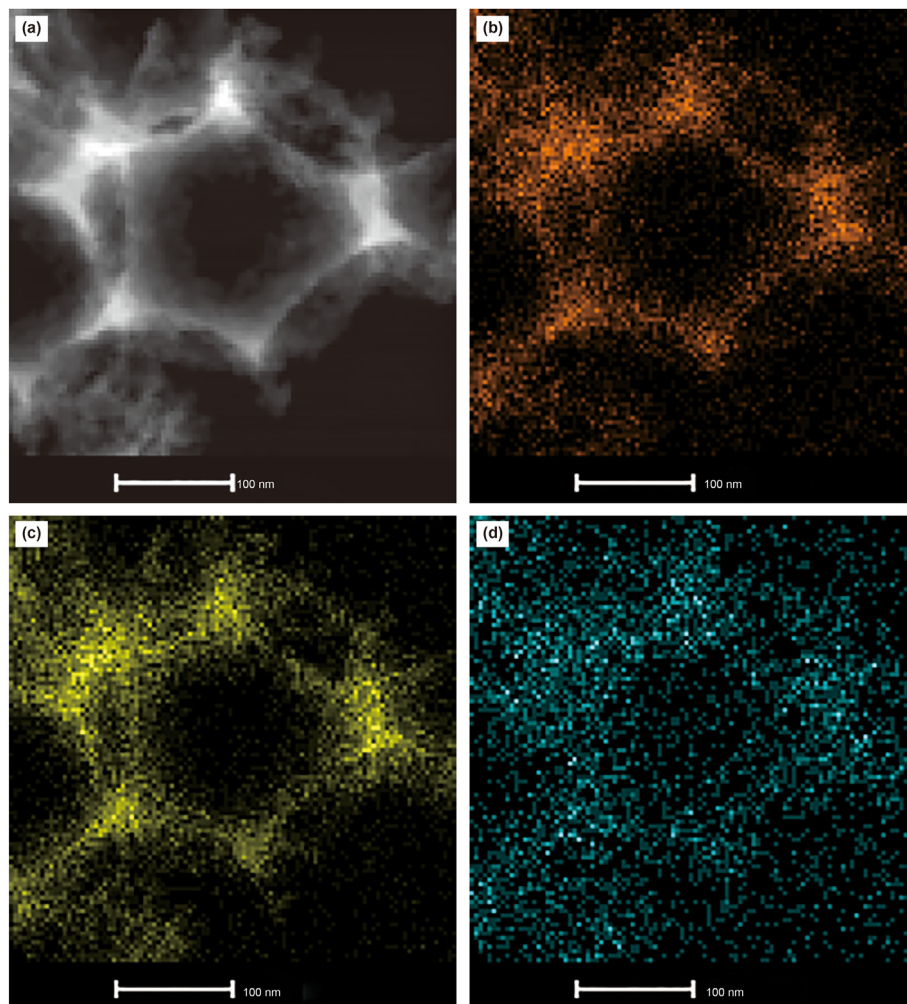
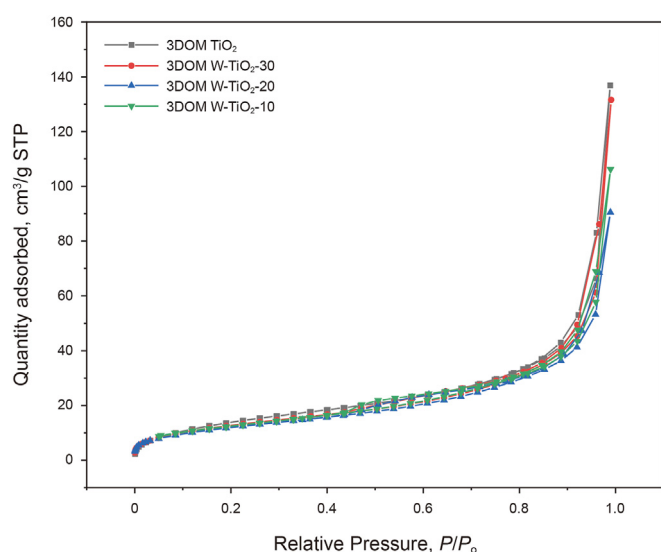**Fig. 6.** TEM-mapping images of 3DOM W–TiO$_2$-20.

Fig. 7. Nitrogen adsorption-desorption isotherms of the as-prepared materials.

3.2. Catalytic activity performance

The aerobic oxidative desulfurization performance of various samples is investigated under the same reaction condition (Fig. 8). For 3DOM TiO$_2$, the sulfur removal could reach 50% in 6 h. After the introduction of tungsten, 3DOM W–TiO$_2$-20 exhibited the highest activity with a sulfur removal of 98%. For 3DOM W–TiO$_2$-10 with higher tungsten content, the desulfurization activity decreased compared to 3DOM W–TiO$_2$-20, which was ascribed to the lower pore volume in the sample (Table 1). In addition, the sulfur removal of 3DOM W–TiO$_2$-30 was slightly lower than that of 3DOM W–TiO$_2$-20, which was attributed to the lower tungsten content.

ODS performance on different sulfur-containing compounds is also investigated under the same experimental conditions (Fig. 9). It can be found that the desulfurization activity decreased in the order of DBT > 4-MDBT > 4,6-DMDBT. For DBT, the desulfurization rate can reach 98% in 6 h, while it takes 8 h for 4-MDBT. For 4,6-DMDBT, the sulfur removal only could reach 79% in 8 h. The difference on the activity was ascribed to the steric hindrance of the sulfur atoms in the sulfur compounds (Wang et al., 2020a). The steric hindrance of sulfur atoms in the different sulfur compounds was decreased in the order of 4,6-DMDBT > 4-MDBT > DBT. Sulfur atoms with low steric hindrance exhibited higher catalytic activity. The results indicated that the ODS performance was primarily affected by the steric hindrance of the sulfur atoms in the desulfurization process (Zhang et al., 2019).

Table 1
Textural properties of different samples.

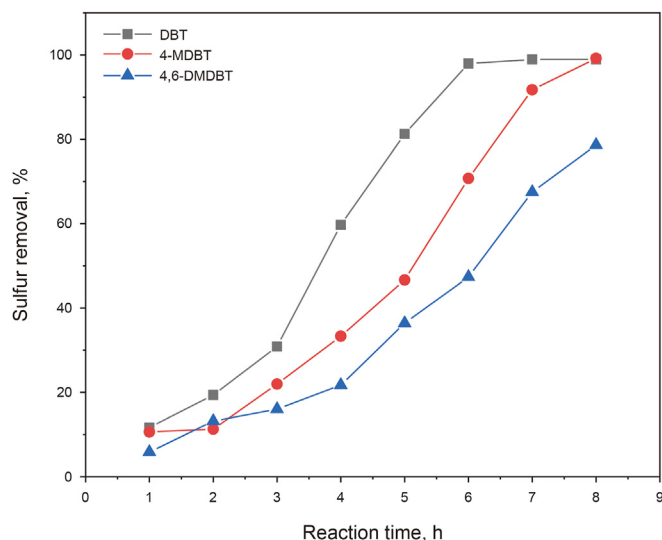| Entry	Samples	BET Surface Area, m^2/g	Pore Volume, cm^3/g
1	3DOM TiO$_2$	53.6	0.21
2	3DOM W–TiO$_2$-30	46.9	0.20
3	3DOM W–TiO$_2$-20	45.4	0.14
4	3DOM W–TiO$_2$-10	44.4	0.06
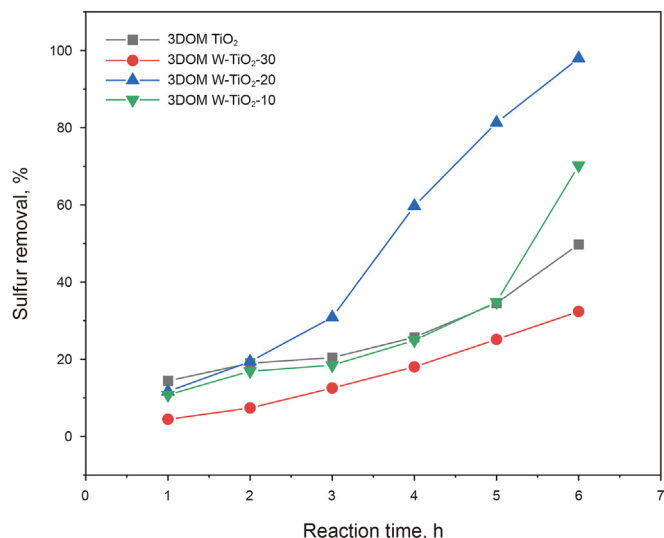
Fig. 8. ODS performance of various samples.
Reaction conditions: m (catalyst) = 0.01 g, V (oil) = 20 mL, T = 120 °C, v (air) = 100 mL min^{-1}.

Fig. 9. ODS performance different substrates.
Reaction conditions: m (catalyst) = 0.01 g, V (oil) = 20 mL, T = 120 °C, v (air) = 100 mL min^{-1}.

Moreover, the recycling performance of the sample 3DOM W–TiO$_2$-20 is also investigated in this study (Fig. 10). After reaction, the upper oil phase was directly separated by decantation, and the catalyst was then transferred to an oven and dried at 80 °C for 8 h. In the next reaction, the fresh oil was added to the reactor and carried out under the same conditions. After recycling four times, the sulfur removal could still reach 95.2%, demonstrating a good recycling ability.

To investigate the reaction product in the ODS process, oil phase and the extracted phase of the catalyst after reaction are detected via GC-MS analysis (Fig. 11). For the total ion flow (TIF) diagram of the oil phase before reaction (Fig. 11a), the peaks of internal standard hexadecane and DBT could be observed at 5.6 min and 7.3 min respectively. For the oil phase during reaction (Fig. 11b), the peak intensity of DBT declined, demonstrating the successful removal of sulfides from the oil phase. After reaction, the oil phase was separated by decantation, and the lower catalyst was separated by filtration and extracted with tetrachloromethane. In Fig. 11c, the peak of the internal standard (hexadecane) was found, while the peak of the DBT was not observed, indicating the complete removal of DBT. In Fig. 11d, an obvious peak with a mass-to-charge ratio (m/z) of 216 was observed at 11.8 min, corresponding to the oxidation product (DBTO$_2$) (Wang et al. 2021). These results indicated that the sulfur compound was oxidized to its corresponding sulfone in the catalyst phase.

4. Conclusions

To sum up, a series of hybrid materials 3DOM W–TiO$_2$ were successfully prepared via the colloidal crystal template, and
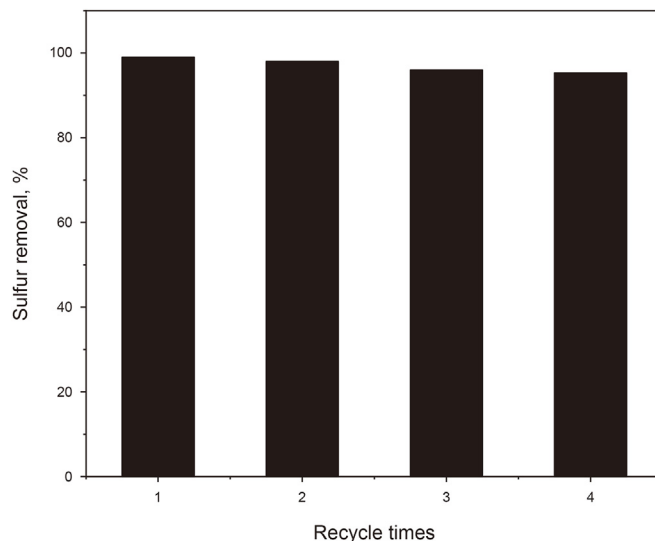
Fig. 10. Recycle performance of the reaction system.
Reaction conditions: m (catalyst) = 0.01 g, V (oil) = 20 mL, T = 120 °C, V (air) = 100 mL min^{-1}.

employed as catalysts for aerobic oxidative desulfurization in fuel. The experimental results indicated that the prepared materials possessed excellent three-dimensional ordered macroporous (3DOM) structure, promoting the oxidative desulfurization process. For the sample 3DOM W–TiO$_2$-20, the sulfur removal could reach 98% in 6 h. After recycling for 4 times, the desulfurization rate could still achieve 95.2% without a significant decrease. For different sulfur compounds under the same condition, the desulfurization rates decreased in the following order of DBT > 4-MDBT > 4,6-DMDBT. This work provided a facile way for the synthesis of 3DOM materials for aerobic oxidative desulfurization in fuel oil.
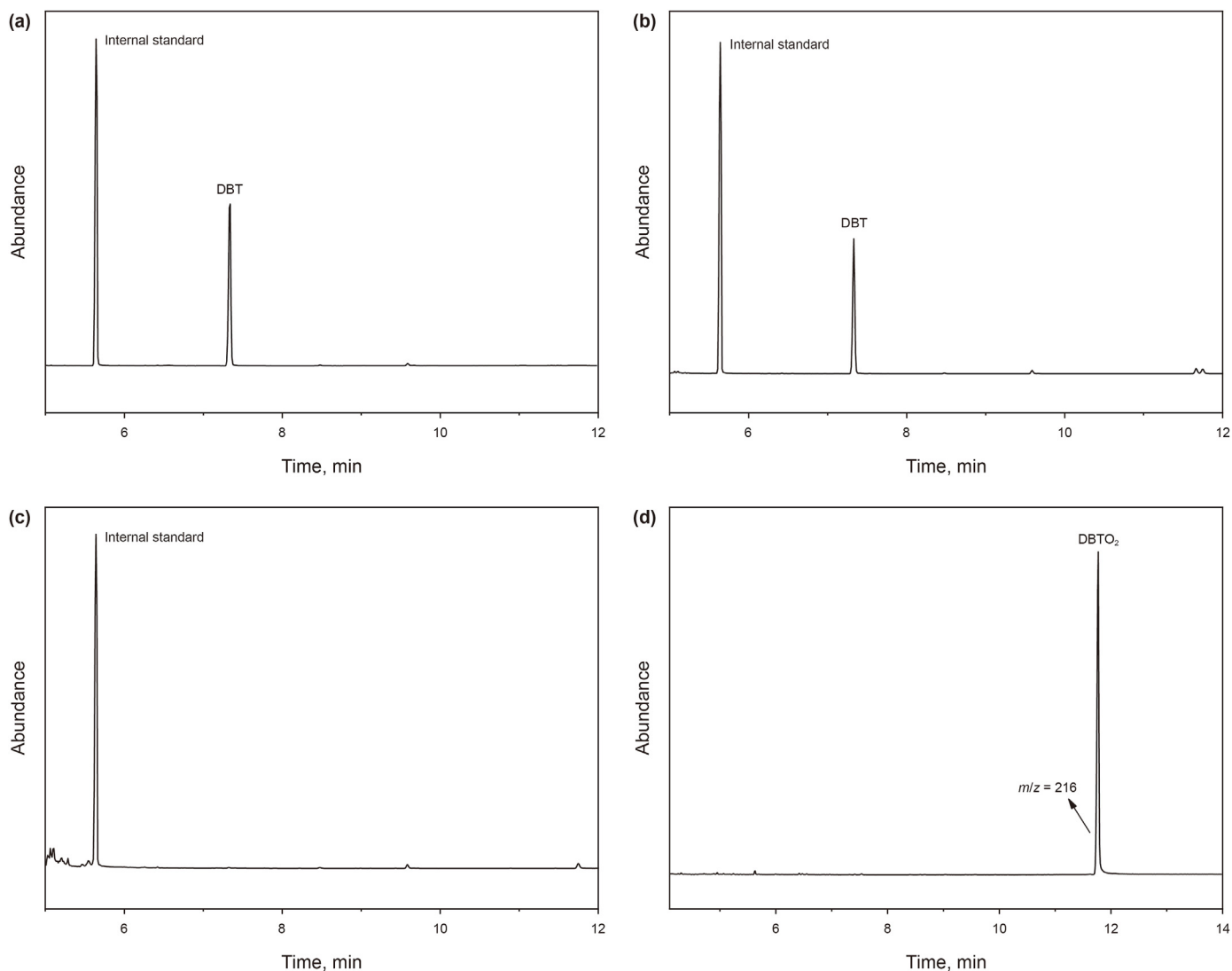
Fig. 11. GC-MS analysis of **a** model oil before reaction, **b** oil phase during reaction, **c** oil phase after reaction and **d** extraction phase of the catalyst after reaction.

References

Ahmed, I., Jhung, S.H., 2016. Adsorptive desulfurization and denitrogenation using metal-organic frameworks. J. Hazard Mater. 301, 259–276. https://doi.org/10.1016/j.jhazmat.2015.08.045.

Cao, H., Bai, Z., Li, Y., et al., 2020. Solvothermal synthesis of defect-rich mixed 1T-2H MoS2 nanoflowers for enhanced hydrodesulfurization. ACS Sustain. Chem. Eng. 8 (19), 7343–7352. https://doi.org/10.1021/acssuschemeng.0c00736.

Celestine, A.D.N., Beiermann, B.A., May, P.A., et al., 2014. Fracture-induced activation in mechanophore-linked, rubber toughened PMMA. Polymer 55 (16), 4164–4171. https://doi.org/10.1016/j.polymer.2014.06.019.

Chen, K., Liu, N., Zhang, M., et al., 2017. Oxidative desulfurization of dibenzothiophene over monoclinic VO2 phase-transition catalysts. Appl. Catal., B 212, 32–40. https://doi.org/10.1016/j.apcatb.2017.04.046.

Chen, X., Liu, W., Tang, L., et al., 2014. Electrochemical sensor for detection of hydrazine based on Au@Pd core-shell nanoparticles supported on amino-functionalized TiO2 nanotubes. Mater. Sci. Eng. C 34, 304–310. https://doi.org/10.1016/j.msec.2013.09.016.

Chi, M., Su, T., Sun, L., et al., 2020. Biomimetic oxygen activation and electron transfer mechanism for oxidative desulfurization. Appl. Catal., B 275, 119134. https://doi.org/10.1016/j.apcatb.2020.119134.

Colusso, A., Cortie, M.B., Dowd, A., et al., 2017. Thermal stability of mesoscopic compounds of cetyltrimethylammonium and Keggin metatungstates. Dalton Trans. 46 (33), 11053–11062. https://doi.org/10.1039/c7dt02073b.

Cong, Y., Li, X., Qin, Y., et al., 2011. Carbon-doped TiO2 coating on multiwalled carbon nanotubes with higher visible light photocatalytic activity. Appl. Catal., B 107 (1–2), 128–134. https://doi.org/10.1016/j.apcatb.2011.07.005.

Dong, L., Miao, G., Ren, X., et al., 2020. Desulfurization kinetics and regeneration of silica gel-supported TiO2 extrudates for reactive adsorptive desulfurization of real diesel. Ind. Eng. Chem. Res. 59 (21), 10130–10141. https://doi.org/10.1021/acs.iecr.0c00942.

Du, Y., Lei, J., Zhou, L., et al., 2018. Highly efficient deep desulfurization of fuels by meso/macroporous H3PW12O40/TiO2 at room temperature. Mater. Res. Bull. 105, 210–219. https://doi.org/10.1016/j.materresbull.2018.04.048.

Hao, Y., Hao, Y.J., Ren, J., et al., 2019. Extractive/catalytic oxidative mechanisms over [Hnmp]Cl·xFeCl3 ionic liquids towards the desulfurization of model oils. New J. Chem. 43 (20), 7725–7732. https://doi.org/10.1039/c9nj00691e.

He, J., Wu, P., Wu, Y., et al., 2017. Taming interfacial oxygen vacancies of amphiphilic tungsten oxide for enhanced catalysis in oxidative desulfurization. ACS Sustain. Chem. Eng. 5 (10), 8930–8938. https://doi.org/10.1021/acssuschemeng.7b01741.

Jiang, B., Yang, H., Zhang, L., et al., 2016. Efficient oxidative desulfurization of diesel fuel using amide-based ionic liquids. Chem. Eng. J. 283, 89–96. https://doi.org/10.1016/j.cej.2015.07.070.

Li, J.J., Xiao, H., Tang, X.D., et al., 2016. Green carboxylic acid-based deep eutectic solvents as solvents for extractive desulfurization. Energy Fuels 30 (7), 5411–5418. https://doi.org/10.1021/acs.energyfuels.6b00471.

Li, Y., Song, J., Jiang, M., et al., 2020. The fabrication of IMo6@iPAF-1 as an enzyme mimic in heterogeneous catalysis for oxidative desulfurization under O_2 or air. J. Mater. Chem. 8 (19), 9813–9824. https://doi.org/10.1039/c9ta14066b.

Pei, W., Dai, L., Liu, Y., et al., 2020. PtRu nanoparticles partially embedded in the 3DOM $Ce_{0.7}Zr_{0.3}O_2$ skeleton: active and stable catalysts for toluene combustion. J. Catal. 385, 274–288. https://doi.org/10.1016/j.jcat.2020.02.028.

Saleh, T.A., Al-Hammadi, S.A., Al-Amer, A.M., 2019. Effect of boron on the efficiency of MoCo catalysts supported on alumina for the hydrodesulfurization of liquid fuels. Process Saf. Environ. 121, 165–174. https://doi.org/10.1016/j.psep.2018.10.019.

Shen, J.Y., Wang, M.D., Wang, Y.F., et al., 2018. Iron and carbon codoped WO_3 with hierarchical walnut-like microstructure for highly sensitive and selective acetone sensor. Sensor. Actuator. B 256, 27–37. https://doi.org/10.1016/j.snb.2017.10.073.

Soltani, R., Marjani, A., Shirazian, S., 2019. Facile one-pot synthesis of thiol-functionalized mesoporous silica submicrospheres for Tl(I) adsorption: isotherm, kinetic and thermodynamic studies. J. Hazard Mater. 371, 146–155. https://doi.org/10.1016/j.jhazmat.2019.02.076.

Song, Z., Zhou, T., Qi, Z., et al., 2017. Systematic method for screening ionic liquids as extraction solvents exemplified by an extractive desulfurization process. ACS Sustain. Chem. Eng. 5 (4), 3382–3389. https://doi.org/10.1021/acssuschemeng.7b00024.

Sousa, J.P.M., Neves, R.P.P., Sousa, S.F., et al., 2020. Reaction mechanism and determinants for efficient catalysis by DszB, a key enzyme for crude oil biodesulfurization. ACS Catal. 10 (16), 9545–9554. https://doi.org/10.1021/acscatal.0c03122.

Sun, H.B., Wu, P.W., He, J., et al., 2018. Fabrication of oxygen-defective tungsten oxide nanorods for deep oxidative desulfurization of fuel. Petrol. Sci. 15 (4), 849–856. https://doi.org/10.1007/s12182-018-0265-7.

Tan, P., Xie, X.Y., Liu, X.Q., et al., 2017. Fabrication of magnetically responsive HKUST-1/Fe_3O_4 composites by dry gel conversion for deep desulfurization and denitrogenation. J. Hazard. Mater. 321, 344–352. https://doi.org/10.1016/j.jhazmat.2016.09.026.

Ullah, H., Haider, A., Khalid, N., et al., 2018. Tuning the band gap of TiO_2 by tungsten doping for efficient UV and visible photodegradation of Congo red dye. Spectrochim. Acta 204, 150–157. https://doi.org/10.1016/j.saa.2018.06.046.

Wang, C., Jiang, W., Xun, S., et al., 2021. Pt nanoparticles encapsulated on V_2O_5 nanosheets carriers as efficient catalysts for promoted aerobic oxidative desulfurization performance. Chin. J. Catal. 42 (4), 557–562. https://doi.org/10.1016/S1872-2067(20)63685-3.

Wang, C., Qiu, Y., Wu, H., et al., 2020a. Construction of 2D-2D V_2O_5/BNNS nanocomposites for improved aerobic oxidative desulfurization performance. Fuel 270, 117498. https://doi.org/10.1016/j.fuel.2020.117498.

Wang, C., Yi, Y., Li, H., et al., 2020b. Rapid gas-assisted exfoliation promises V_2O_5 nanosheets for high performance lithium-sulfur batteries. Nano Energy 67, 104253. https://doi.org/10.1016/j.nanoen.2019.104253.

Wang, J., Song, Z., Li, X., et al., 2020. Toward rational functionalization of ionic liquids for enhanced extractive desulfurization: computer-aided solvent design and molecular dynamics simulation. Ind. Eng. Chem. Res. 59 (5), 2093–2103. https://doi.org/10.1021/acs.iecr.9b05684.

Wei, Y., Li, G., Yi, Y., et al., 2020. An octane mediated strategy towards Ti-containing HMS-type mesoporous materials incorporated with methyl for high-efficiency oxidative desulfurization. Fuel 280, 118660. https://doi.org/10.1016/j.fuel.2020.118660.

Wu, Q., Jing, M., Wei, Y., et al., 2019. High-efficient catalysts of core-shell structured Pt@transition metal oxides (TMOs) supported on 3DOM-Al_2O_3 for soot oxidation: the effect of strong Pt-TMO interaction. Appl. Catal., B 244, 628–640. https://doi.org/10.1016/j.apcatb.2018.11.094.

Xiao, J., Wu, L., Wu, Y., et al., 2014. Effect of gasoline composition on oxidative desulfurization using a phosphotungstic acid/activated carbon catalyst with hydrogen peroxide. Appl. Energy 113, 78–85. https://doi.org/10.1016/j.apenergy.2013.06.047.

Xie, S., Bi, Z., Chen, Y., et al., 2018. Electrodeposited Mo-doped WO_3 film with large optical modulation and high areal capacitance toward electrochromic energy-storage applications. Appl. Surf. Sci. 459, 774–781. https://doi.org/10.1016/j.apsusc.2018.08.045.

Xie, S., Deng, J., Zang, S., et al., 2015. Au-Pd/3DOM Co_3O_4: highly active and stable nanocatalysts for toluene oxidation. J. Catal. 322, 38–48. https://doi.org/10.1016/j.jcat.2014.09.024.

Xiong, J., Yang, L., Chao, Y., et al., 2016. Boron nitride mesoporous nanowires with doped oxygen atoms for the remarkable adsorption desulfurization performance from fuels. ACS Sustain. Chem. Eng. 4 (8), 4457–4464. https://doi.org/10.1021/acssuschemeng.6b01156.

Xu, J., Zhu, Z., Su, T., et al., 2020. Green aerobic oxidative desulfurization of diesel by constructing an Fe-Anderson type polyoxometalate and benzene sulfonic acid-based deep eutectic solvent biomimetic cycle. Chin. J. Catal. 41 (5), 868–876. https://doi.org/10.1016/S1872-2067(19)63500-X.

Xun, S., Jiang, W., Guo, T., et al., 2019. Magnetic mesoporous nanospheres supported phosphomolybdate-based ionic liquid for aerobic oxidative desulfurization of fuel. J. Colloid Interface Sci. 534, 239–247. https://doi.org/10.1016/j.jcis.2018.08.115.

Xun, S., Zhu, W., Chang, Y., et al., 2016. Synthesis of supported $SiW_{12}O_{40}$-based ionic liquid catalyst induced solvent-free oxidative deep-desulfurization of fuels. Chem. Eng. J. 288, 608–617. https://doi.org/10.1016/j.cej.2015.12.005.

Yang, H., Jiang, B., Sun, Y., et al., 2018. Construction of polyoxometallate-based organic-inorganic hybrid nanowires for efficient oxidative desulfurization. Mol. Catal. 448, 38–45. https://doi.org/10.1016/j.mcat.2018.01.016.

Yang, H., Jiang, B., Sun, Y., et al., 2017. Polymeric cation and isopolyanion ionic self-assembly: novel thin-layer mesoporous catalyst for oxidative desulfurization. Chem. Eng. J. 317, 32–41. https://doi.org/10.1016/j.cej.2017.01.135.

Yang, P., Zhou, S., Du, Y., et al., 2017. Self-assembled meso/macroporous phospho-tungstic acid/TiO_2 as an efficient catalyst for oxidative desulfurization. J. Porous Mater. 24 (2), 531–539. https://doi.org/10.1007/s10934-016-0288-7.

Ye, G., Sun, Y., Zhang, D., et al., 2018. Hierarchical porous titanium terephthalate based material with highly active sites for deep oxidative desulfurization. Microporous Mesoporous Mater. 270, 241–247. https://doi.org/10.1016/j.micromeso.2018.05.025.

Yuan, P., Liu, J., Li, Y., et al., 2014. Effect of pore diameter and structure of mesoporous sieve supported catalysts on hydrodesulfurization performance. Chem. Eng. Sci. 111, 381–389. https://doi.org/10.1016/j.ces.2014.03.006.

Zalfani, M., van der Schueren, B., Mandouani, M., et al., 2016. ZnO quantum dots decorated 3DOM TiO_2 nanocomposites: symbiose of quantum size effects and photonic structure for highly enhanced photocatalytic degradation of organic pollutants. Appl. Catal., B 199, 187–198. https://doi.org/10.1016/j.apcatb.2016.06.016.

Zhang, M., Liu, J., Li, H., et al., 2020. Tuning the electrophilicity of vanadium-substituted polyoxometalate based ionic liquids for high-efficiency aerobic oxidative desulfurization. Appl. Catal., B 271, 118936. https://doi.org/10.1016/j.apcatb.2020.118936.

Zhang, M., Liu, J., Yang, J., et al., 2019. Molybdenum-containing dendritic mesoporous silica spheres for fast oxidative desulfurization in fuel. Inorg. Chem. Front. 6 (2), 451–458. https://doi.org/10.1039/c8qi00987b.

Zhang, M., Wei, Y., Li, R., et al., 2017. Magnetic POM-based mesoporous silica for fast oxidation of aromatic sulfur compounds. Fuel 209, 545–551. https://doi.org/10.1016/j.fuel.2017.08.001.

Zhang, M., Zhu, W., Xun, S., et al., 2013. Deep oxidative desulfurization of dibenzothiophene with POM-based hybrid materials in ionic liquids. Chem. Eng. J. 220, 328–336. https://doi.org/10.1016/j.cej.2012.11.138.